Available online at www.sciencedirect.com
ScienceDirect
Trans. Nonferrous Met. Soc. China 33(2023) 2090−2109
Transactions of Nonferrous Metals Society of China
www.tnmsc.cn

Effect of laser surface melting on microstructure evolution and cavitation behavior of nickel aluminum bronze

Si-qi ZENG, Jing-jing TIAN, Shu-bing HU, Ming XIAO, Bo PENG

State Key Laboratory of Material Processing and Die and Mould Technology,
School of Materials Science and Engineering, Huazhong University of Science and Technology, Wuhan 430074, China

Received 7 August 2022; accepted 19 April 2023

Abstract: The laser surface melting was employed on the nickel aluminum bronze to augment the cavitation performance. To investigate the effect of laser treatment, the microstructure was characterized by X-ray diffraction, scanning electron microscopy, and transmission electron microscopy. And the cavitation behavior was tested on an ultrasonic vibratory machine. The results show that the optimal process parameter with laser power of 3 kW and scanning speed of 10 mm/s contributes to the increased corrosion resistance and reduced cavitation mass loss, compared with the cast sample, respectively. The enhancement of the cavitation resistance is dominated by the synergistic mechanism of grain refinement strengthening, dislocation strengthening, and precipitate strengthening, with the homogeneous structure eliminating selective corrosion.

Key words: nickel aluminum bronze; laser surface melting; precipitates; dislocation

1 Introduction

Nickel aluminum bronze (NAB) is extensively used in marine engineering structures for superior mechanical properties, processability, and corrosion resistance. NAB contains multiple phases, such as α and κ phases. The α phase has a face-centered cubic lattice, exhibiting the highest plasticity among all the phases. The (Fe,Ni)-rich κ mainly consists of Al−Fe and Al−Ni compounds, such as $FeAl_3$ and NiAl, while exhibiting the highest hardness of about HV 530. The κ phase is distributed in various forms, such as the rosette (κ_{I}), globular (κ_{II}), and lamellar (κ_{III}) forms, or as a fine precipitate within the α phase (κ_{IV}) [1,2]. NAB is prone to cavitation corrosion working in seawater [3]. When the propellers run at high speed, the seawater is tripped and flows rapidly, resulting in many bubbles. The bubbles grow and collapse in the seawater. When bubbles burst on the blades, the jet flow and shock wave cause a hammer force and severe damage to the metals. Many studies on cavitation corrosion show that metals suffer from mechanical shock and chemical corrosion [4−6]. The α phase is mechanically attacked and chemically corroded at the interfaces among the κ phases. In contrast, the κ precipitates around the attacked α phase would be removed during the mechanical shock. The synergistic effect of the corrosion and mechanical attack dominates the cavitation behavior of the alloys [7].

Considerable investigations have been performed on alloys to enhance the cavitation resistance by improving the corrosion resistance and mechanical strength [8]. SONG et al [9] produced a cladding layer on the cast manganese aluminum bronze. The results showed that the clad metals had a lower corrosion and cavitation rate than the cast metals, attributed to the refined grains

Corresponding author: Shu-bing HU, Tel/Fax: +86-27-87540057, E-mail: hushubing@163.com
DOI: 10.1016/S1003-6326(23)66246-6

and homogeneous distribution of the κ phase. YANG et al [10,11] modified the microstructure of NAB by friction stir processing at different processing parameters. The fine and homogeneous layer contributed to the slight cavitation damage by hindering the propagation of the cracks. The mass loss of cavitation after modification at a rotation rate of 1200 and 800 r/min was reduced by 17.6% and 55.9%, respectively. The structure of the specimen with rotation rate of 800 r/min was more homogeneous than that of the specimen with rotation rate of 1200 r/min, resulting in a higher cavitation resistance. THAPLIYAL and DWIVEDI [12] investigated the cavitation performance of NAB after friction stir processing and discussed the effect of the tool parameters on cavitation performance. The results suggested that the refined grain size and surface hardening improve the cavitation resistance. SUN et al [13] used the electropulsing-assisted ultrasonic surface rolling process to obtain a strengthened layer with hardness of HV 267, 67% increase compared to that of the substrate. The mass loss after cavitation was reduced by 47% compared to the substrate, resulting from the strengthened layer. As reported previously, the grain refinement and homogeneous phase structure improve the corrosion resistance and mechanical strength, enhancing the cavitation resistance. Laser surface treatment [14−16] has been reported to modify the surface structure and strengthen mechanical properties. TANG et al [17,18] studied the effect of the laser surface melting on the cavitation behaviors on a copper alloy. A homogeneous layer of a single phase was obtained, eliminating selective corrosion, improving the surface strength, and enhancing cavitation resistance. MITELEA et al [19] investigated the cavitation performance of laser-melted gray cast iron in tap water. The results showed that the melted gray cast iron had higher cavitation resistance, about two times that of the as-received metals, with the hardness increasing from HV 190 to HV 700. With the processed current increasing from 60 to 90 A, the erosion penetration decreased, and the cavitation resistance increased.

It is noted that the laser surface melting (LSM) [20] could enhance the cavitation erosion resistance. However, the cavitation performance differs after the laser treatment because of the differences in the laser parameters (laser power and scanning speed) and test methods. Therefore, optimizing the laser parameters and establishing the relationship among the specific microstructures have industrial value and guiding significance. In this work, the cast NAB was laser melted with different parameters. In addition, the microstructure evolution during LSM at the optimized parameter and the coupling strengthening mechanism of LSM on cavitation resistance were also discussed.

2 Experimental

2.1 Materials processing

The NAB used in the study had a chemical composition (wt.%) of 9.89Al−4.86Fe−4.63Ni−2.02Mn−(bal.)Cu. Before the LSM process, the samples were ground with different grades of SiC paper (from 400# to 1200#). The LSM process was performed on CO_2 laser device (DJ−HL−T5000B). The laser focal point rested 30 mm above the sample surface with a defocusing of 7 mm and a facula area of 10 mm × 1 mm. The LSM parameters are given in Table 1, and the LSM processed NAB (LNAB) specimens would be named "Power-Speed".

Table 1 Laser surface melting parameters of different samples

Power/kW	Speed/(mm·s^{-1})
3, 3.5	5, 10, 15, 20

2.2 Microstructure characterization and microhardness test

According to the standard metallographic sample preparation process, the samples were cut with dimensions of 10 mm × 10 mm × 10 mm for further characterization. The samples were observed by X-ray diffraction (XRD) to get the Bragg diffraction angle distribution patterns. After being polished with SiC paper, the pieces were electrolytically polished at room temperature under 4 V for 30 s; the samples were observed by a field emission scanning electron microscope (FSEM, FEI Nano450) to obtain the structure and composition. After ion etching, the pieces were tested by an electron backscatter diffraction (EBSD, Zeiss Gemini 300) to get orientation mapping based on the Kikuchi lines. The SPM9700 atomic force microscopy (AFM) instrument was used to obtain

the topography and Volta potential images from polished samples. The samples were burnished with sandpapers (400 to 5000 grit) until the required depth (20−50 μm) was obtained. Then, the slices were cut into discs with a diameter of 3 mm for twin-jet chemical polishing. The slice specimens were observed by a field transmission electron microscope (FTEM, FEI Tecnai G2 F30) to get a high magnification of the microstructure.

The microhardness was measured by a digital microhardness tester (DHV−1000) according to GB/T 9790—2021 [21]. The samples were inlaid with epoxy resin and polished. The indenter was positioned each 50 μm along the depth direction of the laser melted layers, while the applied load was 100 g and the loading time was 15 s. Each position of three different points was measured with a horizontal distance of 50 μm, and the average value of the three points was the hardness.

2.3 Electrochemical corrosion and cavitation test

electrochemical polarization test in 3.5 wt.% NaCl solution at 23 °C was performed in a three-electrode cell using a CorrTest electrochemical workstation according to ASTM Standard G5—94 [22], with a pair of graphite rods as the counter electrode and a saturated calomel electrode as the reference electrode. The specimens used in the test were washed in flowing water, dried, and then their morphology was analyzed using SEM.

The cavitation test was performed on an ultrasonic vibratory machine according to ASTM Standard G32—16 [23]. The vibration frequency and peak amplitudes were 20 Hz and 100 μm, respectively. All the samples were cleaned in acetone, dried in the oven, and weighed by an electronic balance with an accuracy of 0.1 mg. Then, the samples were immersed in 3.5% NaCl solution for the ultrasonic cavitation test for 20 h with a distance of 0.5 mm from the vibratory punch. The samples were weighed after 2, 4, 8, 12, 16, and 20 h. The mass loss of each sample was calculated.

3 Results

3.1 Phase constitution and microstructure

Figure 1(a) shows the XRD patterns of LSM and as-received NAB specimens, showing that the NAB substrate consists of α and κ phases. The four types of the κ phases are mainly composed of Fe_3Al

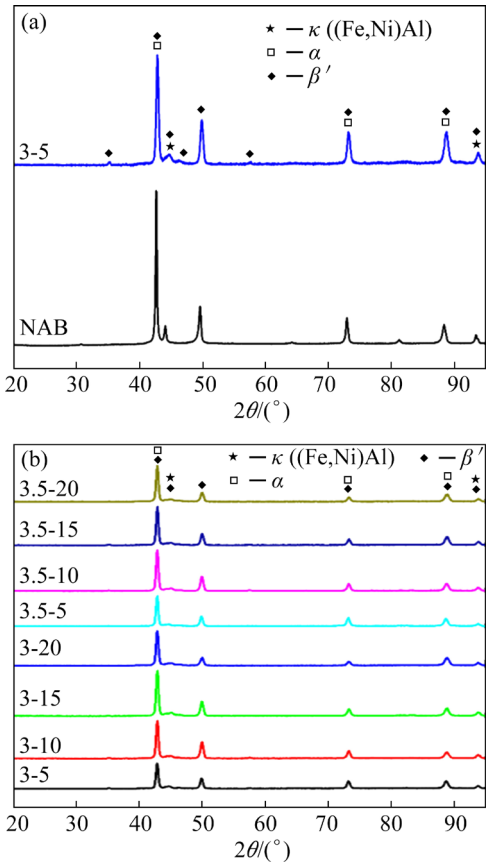

Fig. 1 XRD patterns of NAB and 3-5 specimens (a) and LNAB specimens under different parameters (b)

and NiAl intermetallics, with the same diffraction peaks at 2θ=44.3°, 64.5°, and 81.6°. Therefore, the κ phases are uniformly labeled as a collective phase of (Fe,Ni)Al. The new peaks at 2θ=35°, 42.7°, 44.8°, and 57.1° of the β' phase are found in the patterns of the LNAB specimen in Fig. 1(a). Figure 1(b) shows that the patterns of the LNAB under different laser parameters are similar, with various peak widths. According to the Scherer−Wilson and Williamson−Hall formulas, the relationship between the average crystallite size and full width at half maxima (FWHM) is expressed as [24,25]

$$\beta_D = \frac{K\lambda}{D\cos\theta} \quad (1)$$

where β_D is the broadening of FWHM resulting from the grain refinement. D is the average crystallite size, K is the Scherrer factor, λ is the X-ray wavelength, and θ is the Bragg angle.

Figure 2 shows that the FWHM increases with the laser scanning speed increasing at the same laser power while decreasing with the laser power rising

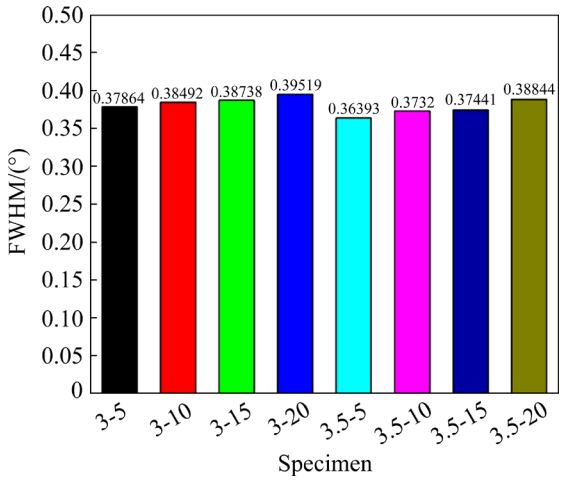

Fig. 2 FWHM of central peak at 2θ=42.7° of LNAB specimens

at the same scanning speed. It is proposed that the average grain size decreases with scanning speed increasing and laser power decreasing, respectively. Specimen 3-20 has the minimum crystallite size, while Specimen 3.5-5 has the maximum.

Figures 3 and 4 show the cross-section microstructures of the NAB and LNAB specimens. The chemical compositions of phases in the NAB and LNAB specimens are given in Table 2. The NAB sample has a heterogeneous microstructure with α phase matrix containing various κ phases. Figure 3(a) shows the coarse κ_{I} phase and the fine κ_{IV} phase appear between and in the α phases. Figure 3(b) shows that the lamellar κ_{III} and globular κ_{II} phases emerge at the α phase boundaries.

The LNAB samples have a homogenous layer of β' phase, a solid solution with a martensitic structure. When the scanning speed is 15 and 20 mm/s, the laser irradiation time of the metals per unit area is too low to afford the complete martensitic transformation. Meanwhile, the energy absorbed on the surface is uneven, resulting in the coarse grains. Furthermore, the κ phase remains undissolved among the boundaries of the β' phase, as shown in Figs. 3(c, d). When the scanning speed is 10 mm/s, the structure is uniform and homogeneous, and the grains are refined, presenting a better LSM effect. When the scanning speed is reduced to 5 mm/s, the metal is irradiated for too long time and absorbs too much energy, resulting in the coarse grain size, as shown in Fig. 3(c). Figure 4 shows the cross-section morphology of the LNAB specimens under the laser power of 3.5 kW. Similarly, at the scanning speed of 15 and 20 mm/s, there are κ phases undissolved among the boundaries of β' phase and coarse grains zone, as shown in Figs. 4(c, d). At the speed of 5 and 10 mm/s, the metals are irradiated sufficiently to complete the martensitic transformation with coarser grains, as shown in Figs. 4(a, b). By comparing Fig. 3 and Fig. 4, the grain size of LNAB alloys presents the same trends consistent with the FWHM results.

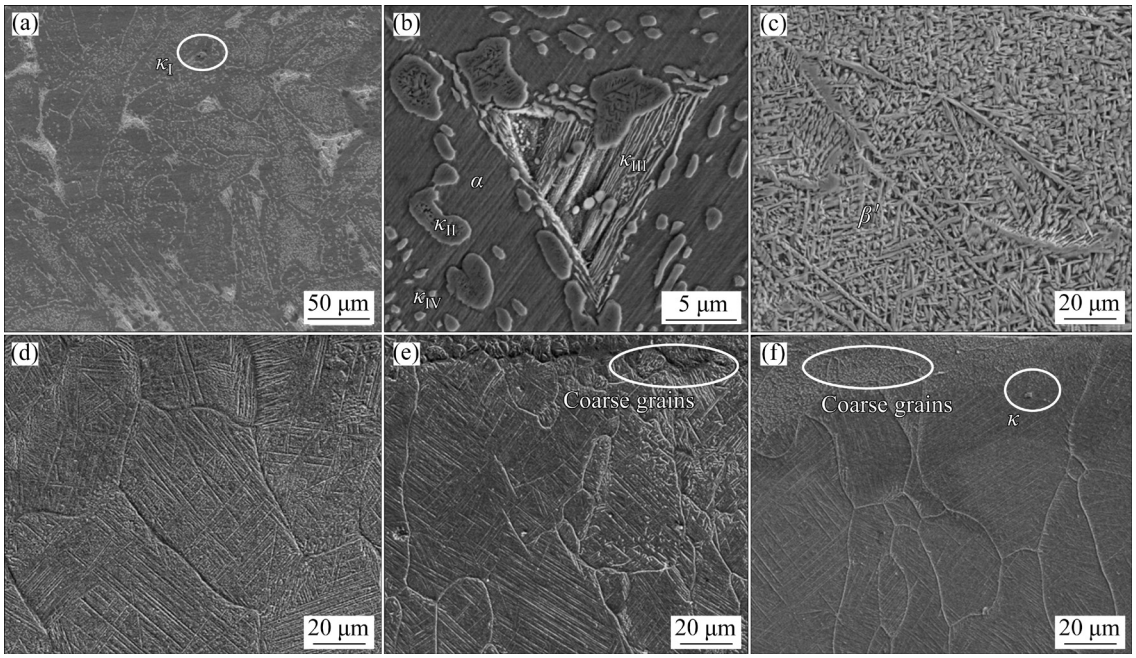

Fig. 3 Microstructures of NAB (a−b), and 3-5 (c), 3-10 (d), 3-15 (e) and 3-20 (f) LNAB specimens

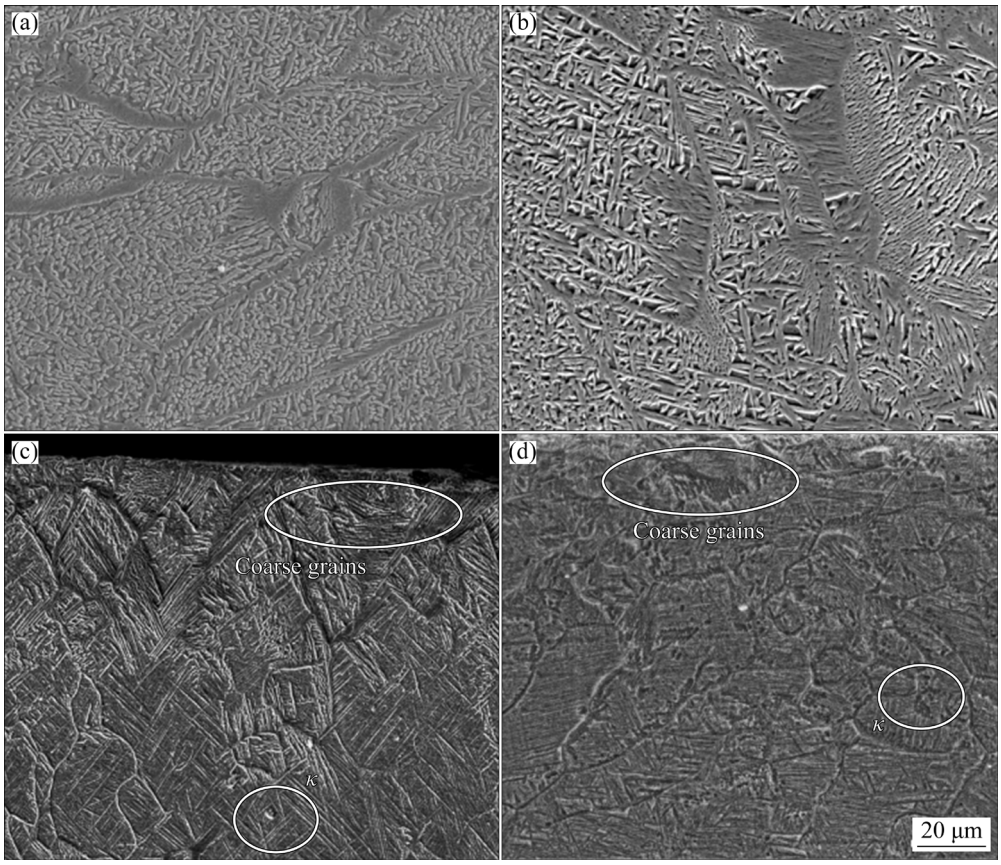

Fig. 4 Microstructures of 3.5-5 (a), 3.5-10 (b), 3.5-15 (c) and 3.5-20 (d) LNAB specimens

Table 2 Chemical composition of each phase of NAB and LNAB specimens (wt.%)

Phase	Chemical composition/wt.%				
	Cu	Al	Fe	Ni	Mn
α	85.47	7.89	2.58	2.05	2.01
κ_{I}	23.39	7.41	57.27	8.51	3.42
κ_{II}	20.91	10.18	58.17	8.20	2.54
κ_{III}	19.78	10.71	31.92	32.73	4.83
κ_{IV}	14.09	10.21	63.42	9.19	3.09
β'	81.17	8.65	3.96	4.12	2.10

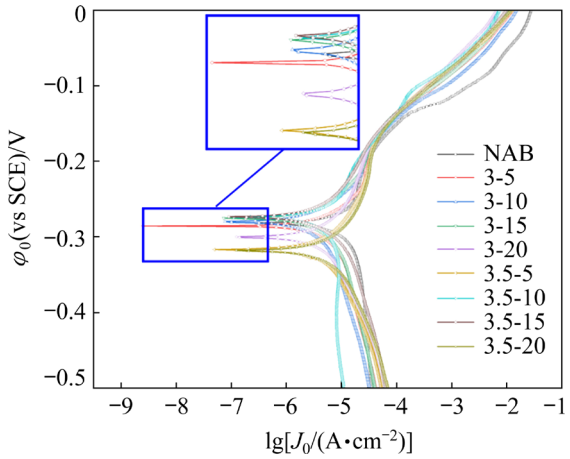

Fig. 5 Potentiodynamic polarization plots of NAB and LNAB specimens

3.2 Electrochemical properties

Figure 5 shows potentiodynamic polarization curves of the NAB and LNAB samples in 3.5% NaCl solution at room temperature. Apart from the shift of the corrosion potential, both sample types show similar corrosion behavior. The cathode reaction is mainly the oxygen reduction reaction [26]. At the applied potential range from −0.303 to −0.265 V, the cathode curve of the NAB sample is almost perpendicular to the vertical axis, indicating diffusion current density limitations. The anodic current density maintains increasing with the potential higher than the initiating passive potential. There is no stable passivation process. The plots of the laser-treated samples present a similar approach to the NAB. According to the Stern−Geary theory, the corrosion potential (φ_{corr}), corrosion current density (J_{corr}), and linear polarization resistance (R_p) are calculated from the plots, and the results using CorrTest software are listed in Table 3. The

Table 3 Electrochemical corrosion parameters of NAB and LNAB specimens

Specimen	φ_{corr}/mV	J_{corr}/(μA·cm^{-2})	R_p/(Ω·cm^{-2})
NAB	−0.28258	16.643	1567.4
3-5	−0.28636	8.5189	3062.3
3-10	−0.28092	5.3423	4883.1
3-15	−0.27599	6.7546	3862.1
3-20	−0.30052	7.0539	3698.2
3.5-5	−0.31693	7.3561	3546.3
3.5-10	−0.27508	8.4089	3102.3
3.5-15	−0.27327	6.9803	3737.2
3.5-20	−0.31813	9.1576	2848.7

polarization resistance of the LNAB samples is significantly improved by 81.7%−211% compared to that of the NAB sample, while the current densities are reduced by about 45.8%−67.9%. The 3-10 specimen presents a higher corrosion resistance resulted from the homogeneous structure and the more refined grains.

The corrosion morphologies of NAB and LNAB specimens under the optimized parameters are shown in Fig. 6. Obvious selective corrosion can be seen on the NAB sample surface which occurs preferentially at the interface of κ_{III} phase and α phase [27−29]. LNAB sample shows uniform corrosion morphology along the martensitic grain boundaries.

3.3 Cavitation performance

Figure 7 shows the calculative mass loss and microhardness of the NAB and LNAB specimens. After LSM, the mass loss of the NAB specimen is reduced after 20 h cavitation erosion. The 3-10 LNAB specimen presents the lowest mass loss in Fig. 7(a). The 3-20 LNAB specimen shows the largest mass losses among the LNAB specimens. The mass loss first decreases and increases as the scanning speed increases under the same laser power. As shown in Fig. 7(b), 3-20 specimen shows the highest peak values but the thinnest strengthened layer, while 3.5-5 specimen has the

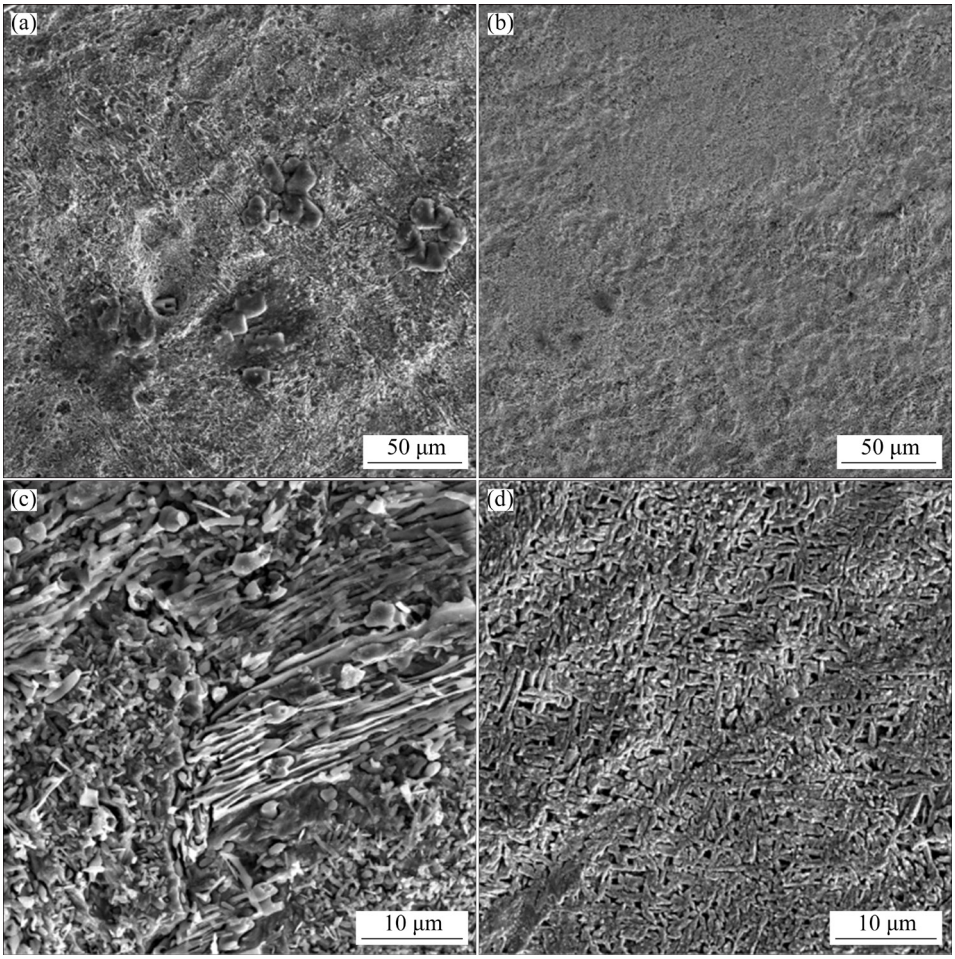

Fig. 6 Corrosion morphologies of NAB (a, c) and LNAB (b, d) specimens

lowest hardness but the thickest reinforced layer. It can be concluded that the peak value decreases and the strengthened layer thickness increases with laser power increasing and scanning speed decreasing. According to the Hall−Petch equation, the micro-hardness distribution is consistent with the grain size regulation.

Figures 8 and 9 show the morphologies of the NAB and LNAB specimens after cavitation erosion. The NAB sample surface suffers severe corrosion and mechanical attack. The cavities emerge on the phase boundaries at the preliminary stage, magnified during the cavitation process, leading to the surface being dismembered and stripped, and presenting an uneven and rough cavitation morphology, as shown in Figs. 8(a, b). The exposed rough surface contributes to more severe corrosion and cavitation erosion. On the contrary, due to the uniform structure, the LNAB alloys suffer relatively uniform damage under the combined action of corrosion and mechanical attack, as shown in Figs. 8 and 9. The refined β' phases are the visible results of the failure mode of layers thinning. In Fig. 8(d), the 3-10 LNAB specimen with the lowest mass loss presents the most stereoscopic β' phase structure for the uniform damage, while the 3-5 LNAB specimen shows more cavities on surface and the 3-15 and 3-20 LNAB specimens have more

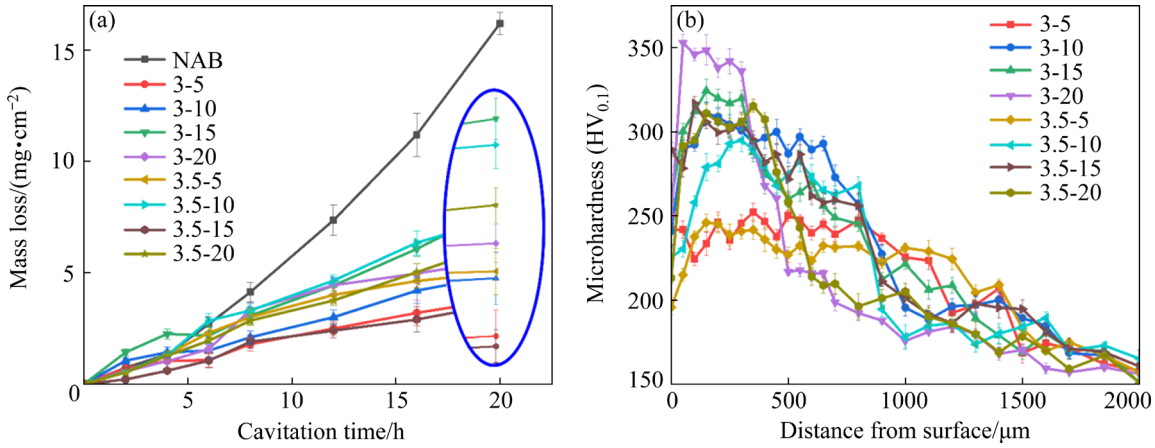

Fig. 7 Mass loss of NAB and LNAB specimens after 20 h cavitation (a), and microhardness distribution along distance from surface of LNAB specimen (b)

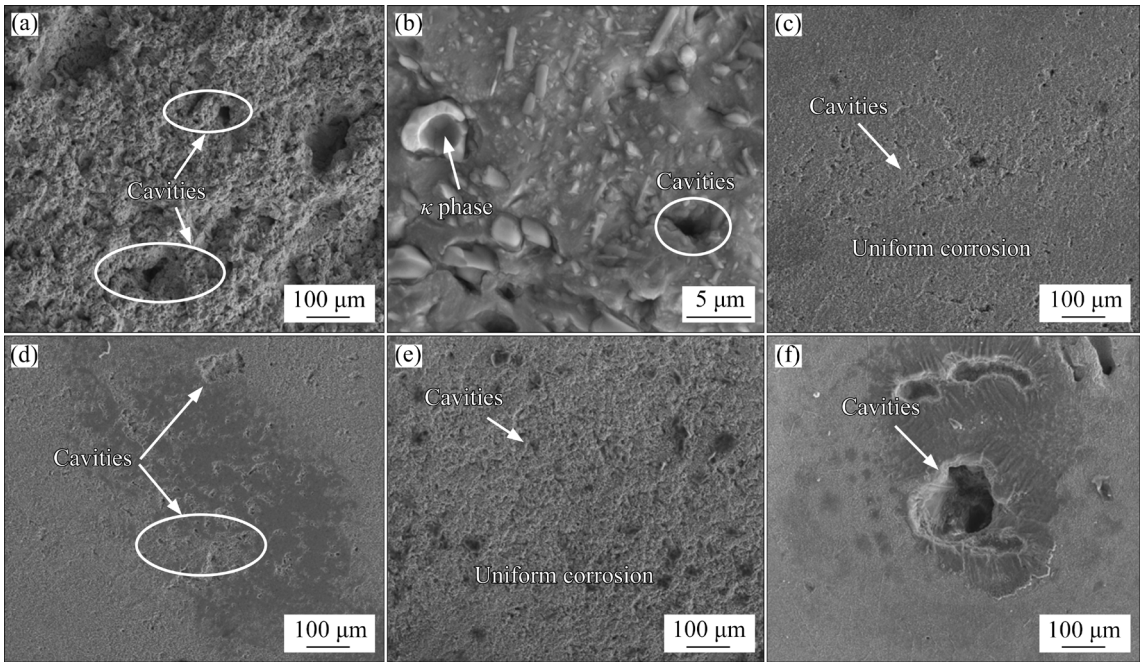

Fig. 8 Morphologies of specimens after 20 h cavitation of NAB (a, b), and 3-5 (c), 3-10 (d), 3-15 (e) and 3-20 (f) LNAB specimens

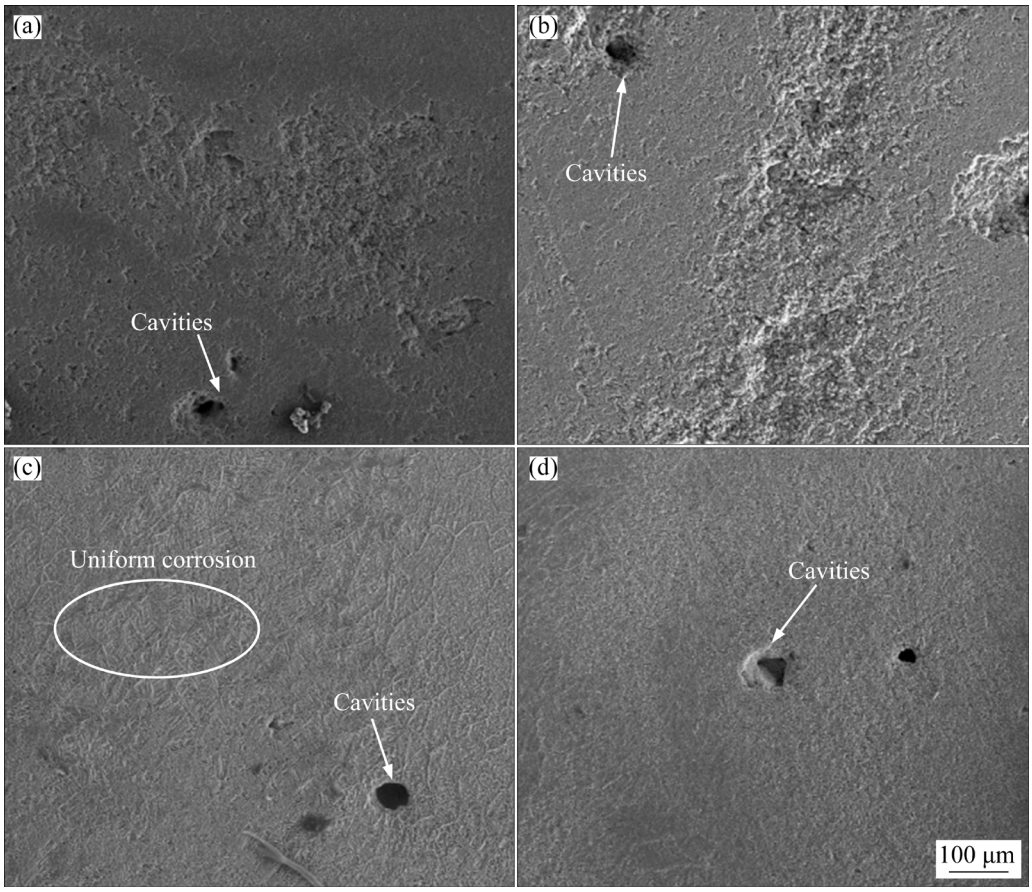

Fig. 9 Morphologies of LNAB specimens after 20 h cavitation: (a) 3.5-5; (b) 3.5-10; (c) 3.5-15; (d) 3.5-20

deep and large holes. Similarly, the 3.5-15 LNAB specimen with the lowest mass loss shows the most apparent lath structure of the β' phase in Fig. 9(c), while other LNAB specimens under the power of 3.5 kW present more and deeper cavities.

4 Discussion

4.1 Microstructure evolution after laser surface melting

Figure 10 shows the microstructures and the inverse pole figures (IPFs) of NAB and 3-10 LNAB specimens. It is found that the complex multiphase structure consists of α phase, and the κ phase is transformed into a single homogeneous martensite β' phase, as shown in Fig. 10(e). The κ phase is represented by the orange spots within and between the α phases in Fig. 10(c). During the process of LSM, the sample surface receives laser energy, with the original α phase as the unit, and forms a collection of blocks with different directions in the process of rapid cooling, showing other colors in the IPF maps in Fig. 10(f).

TEM observations were performed for further investigation, and the results are shown in Fig. 11. It is shown that the κ_{IV} phases dispersively distribute in the α phase (Fig. 11(a)). After LSM, the laths with a width of about 0.5 μm appear, as shown in Fig. 11(b). Figures 11(c, d) show high-magnification images of the laths, indicating that there are precipitates with a size of 10−50 nm with amorphous loops among the laths, which may moderate the difference between the laths and the precipitates. The spherical precipitates are rich in Al and Ni, similar to the substrate. The orientation relationship between lath and precipitate determined from Fig. 11(d) is $(\bar{2}13)_{\mathrm{lath}}//(\bar{2}1\bar{3})_{\mathrm{pre}}$. The other two directions have smaller crystal plan spacing, consistent with the enrichment of Fe, Ni, and Al, with a smaller atomic radius than Cu in the substitutional solid solution.

After LSM, submicron-level parallel laths are the most basic unit of the martensite. And the martensite lath bundles with the same orientation form the blocks. The set of parallel blocks with the same chronic surface are called the packets. Inner

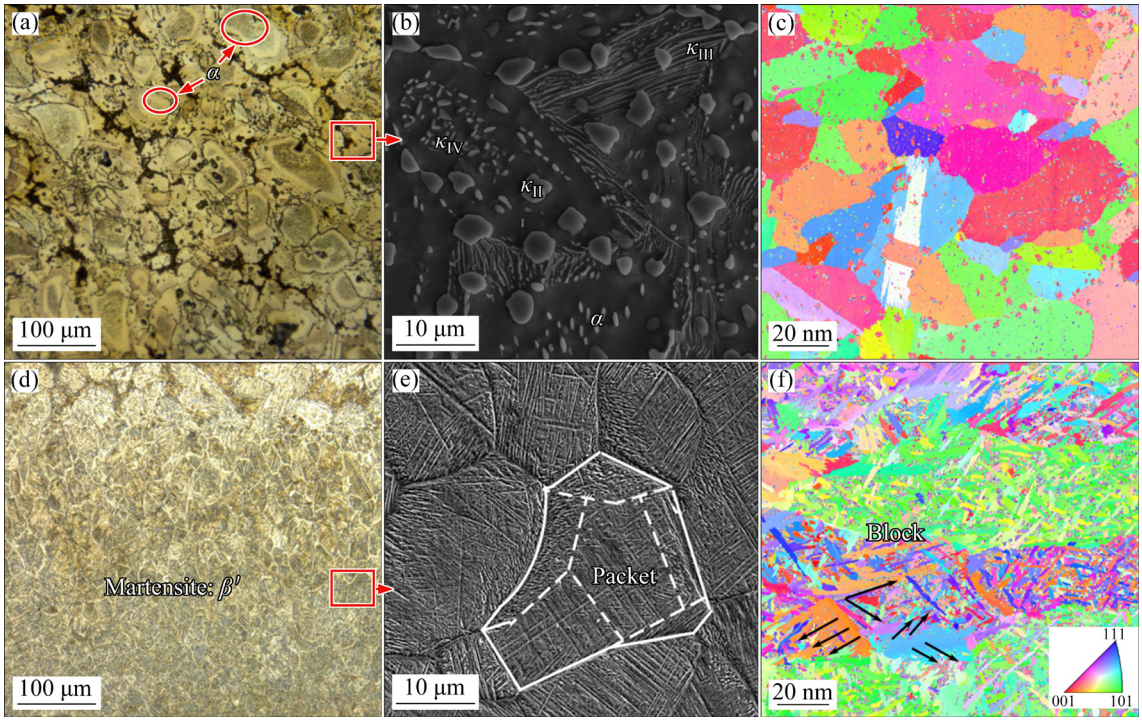

Fig. 10 OM (a, d), SEM (b, e) microstructures and IPFs (c, f) of NAB (a−c) and LNAB (d−f) specimens

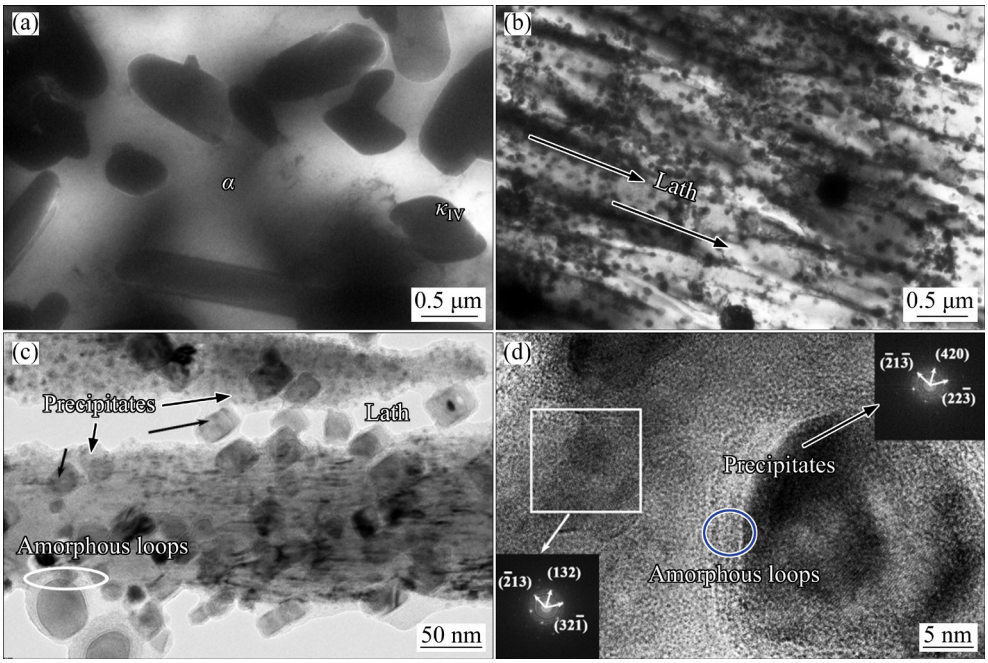

Fig. 11 TEM microstructures of NAB (a) and LNAB (b−d) samples

and original α grain, where there are many packets, and the block boundaries and packet interfaces belong to the large-angle interface. The LNAB has a three-level hierarchy structure consisting of the martensite lath, block, and packet. Meanwhile, there are nanoscale precipitates among the laths, as illustrated in Fig. 12 [30,31].

4.2 Interaction of fine-grain reinforcing and dislocation strengthening

As the dislocations cannot glide through grain boundaries, the boundaries prevent dislocation slips by increasing the shear stress to promote the gliding of interfacial dislocations, which is usually described by the Hall−Petch relationship [32,33]:

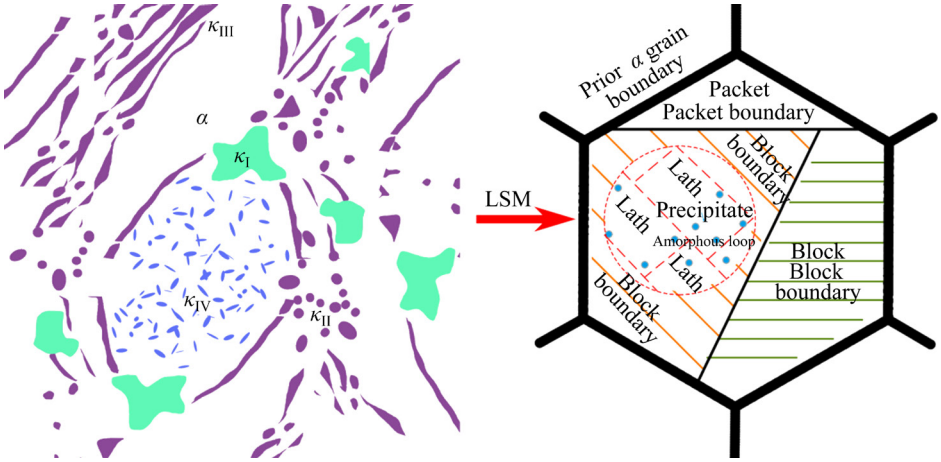

Fig. 12 Schematic illustration of microstructural evolution of NAB sample after LSM

$$\sigma_s=\sigma_0+k_y d^{-1/2} \tag{2}$$

where σ_0 is the critical stress of the sliding surface, which is assumed to be the friction stress for dislocation sliding, k_y is a constant related to lattice type, elastic modulus, dislocation distribution, and degree of dislocation pinning, and d is the grain size. Figure 13 shows IPF maps of the samples, where the color indicates the orientation and the black outlines indicate the grain boundaries. Grain features obtained from the IQ figure show that the grains in the 40 μm area are thicker and shorter than in the 300−900 μm zone. The Hall−Petch relationship shows that grain size determines the material strength, where hardness should decrease with depth increasing for the LNAB sample.

Figure 14 shows the misorientation angle distribution in different regions of the sample. The misorientation angle ranges from 0° to 65° and is clarified into three ranges. The angle <5° indicates the presence of lath misorientation inside the same block; the 5°−55° range indicates packet boundary; the 55°−65° range represents block boundary [34]. Figure 14 shows that the number of sub-grain laths increases while the number of blocks decreases, with increasing depth from the surface, while the fraction of packets stays relatively constant.

Figure 15(a) shows the KAM distribution in the range of 0°−2°. According to the Frank−Bilby theory, the dislocation density (ρ) is proportional to the Kernel average misorientation (KAM) [35,36]:

$$\rho=2\frac{\upsilon}{ub} \tag{3}$$

where υ is the mean KAM value, u is the EBSD constant, and b is the magnitude of Burgers vector of the alloy. Figure 15(b) shows that the dislocation density first increases and then decreases with increasing depth. During the LSM process, the surface region absorbs the most energy, and the dislocations are consumed to form more grains and higher-density interfaces during the formation of martensite lath. Then, with the deepening of the distance, the dislocation density gradually decreases because the absorbed energy gradually decreases, and the dislocation storing energy is steadily consumed to form new grains. The average grain size of the surface layer is 1.7 μm, which is about 1/20 that of the matrix. Therefore, dislocation strengthening and fine grain strengthening show different trends along depth direction.

The flow stress (σ) of the martensite block contains components of dislocation strengthening (σ_{dis}), grain-boundary strengthening (σ_{GB}), and other strengthening mechanisms (σ_{other}) [37]. The term σ_{dis} can be calculated using the Taylor theory [38]:

$$\sigma_{dis}=\alpha M_t G b\sqrt{\rho} \tag{4}$$

where α is the Taylor constant, M_t is the average Taylor factor and $G(=1/2E/(1+\nu))$ is the shear modulus.

Considering Eq. (3), σ_{dis} can be written as

$$\sigma_{dis}=\frac{\alpha M_t E}{2(1+\nu)}\sqrt{\frac{2\upsilon b}{u}} \tag{5}$$

where E is the elastic modulus; ν is the Poisson's ratio.

The contribution of σ_{dis} during the plastic deformation is proportional to M_t and υ. In addition, σ_{GB} is expressed by the Hall−Petch relationship shown in Eq. (2), assuming σ_0=0. Finally, σ_{other} is

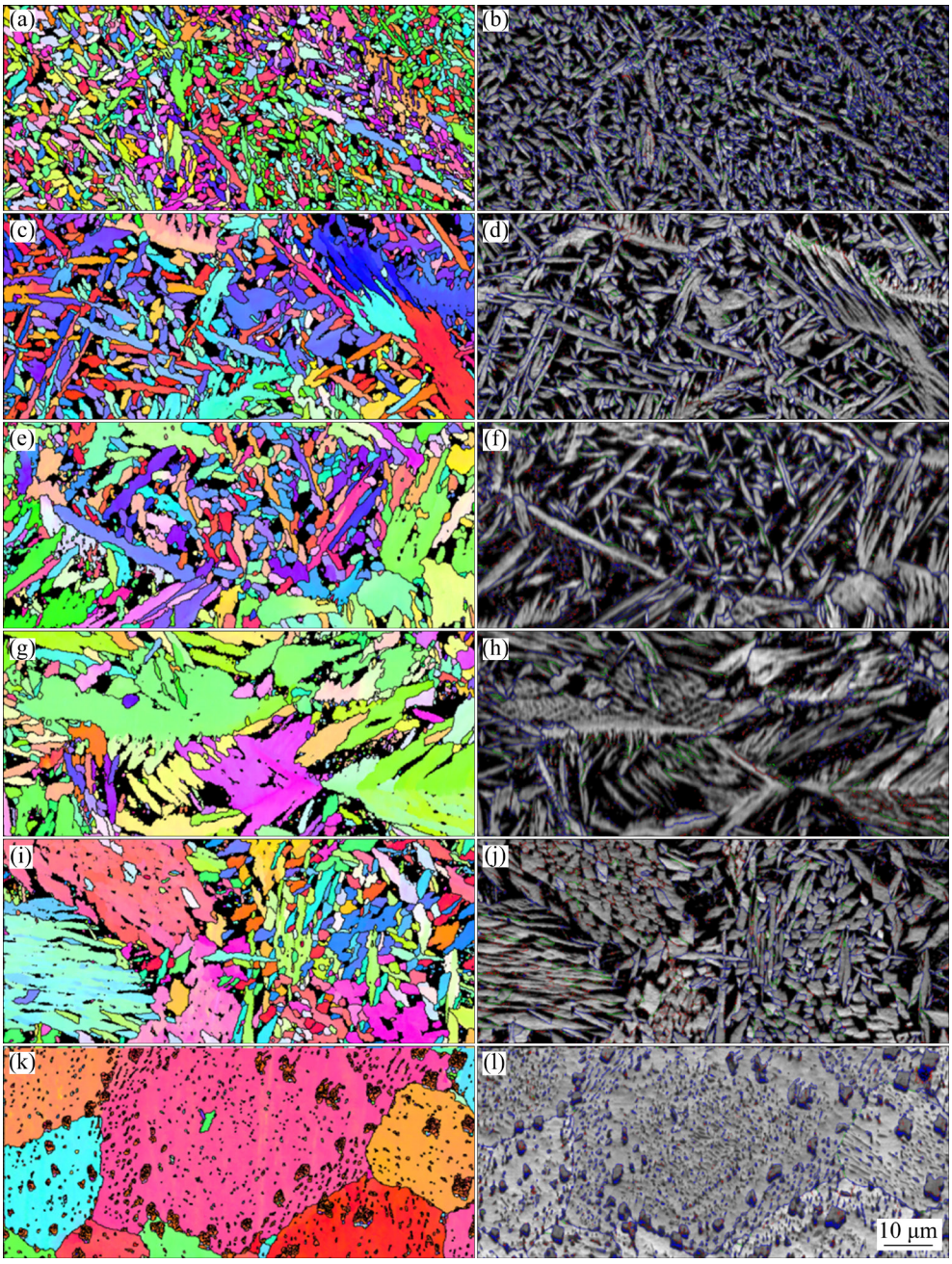

Fig. 13 IPF and IQ maps of regions from surface of different distances: (a, b) 40 μm; (c, d) 300 μm; (e, f) 600 μm; (g, h) 900 μm; (i, j) 1200 μm; (k, l) 4000 μm

depended on the precipitates and solid solution strengthening, and is considered constant during the plastic deformation process. Hence, the final contribution of all stress components can be summarized as follows:

$$\sigma=\frac{\alpha M_{\mathrm{t}} E}{2(1+\nu)}\sqrt{\frac{2\upsilon b}{u}}+\frac{k_{\mathrm{y}}}{\sqrt{d}}+\sigma_{\mathrm{other}} \tag{6}$$

This relationship can accurately predict the strengthening of fine-grain reinforcement and dislocations, with a positive correlation with υ and M_{t} and a negative correlation with d. Equation (6) is applied to the different layers of the LNAB to determine σ_{dis} and σ_{GB} (Table 5). The contribution from σ_{dis} is much more significant than that of σ_{GB} for microscale grain sizes, in good agreement with the specifications of the hardness test. During cavitation, the synergistic effect of refinement and dislocation strengthening at the micrometer scale delays the growth of cavitation crack. It resists the surface plastic deformation, in which dislocation strengthening is dominant.

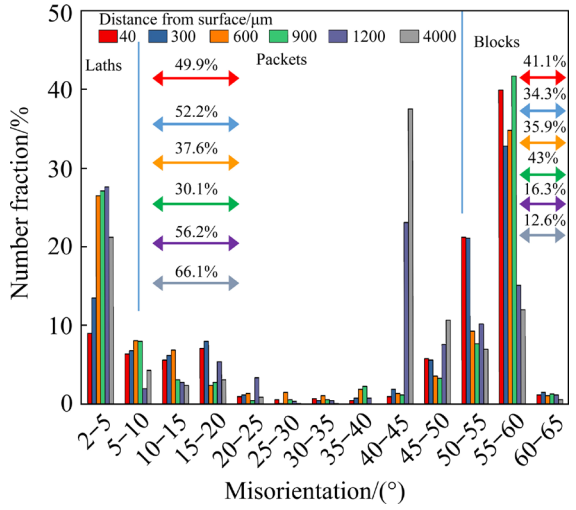

Fig. 14 Misorientation distribution of regions with different distances from surface

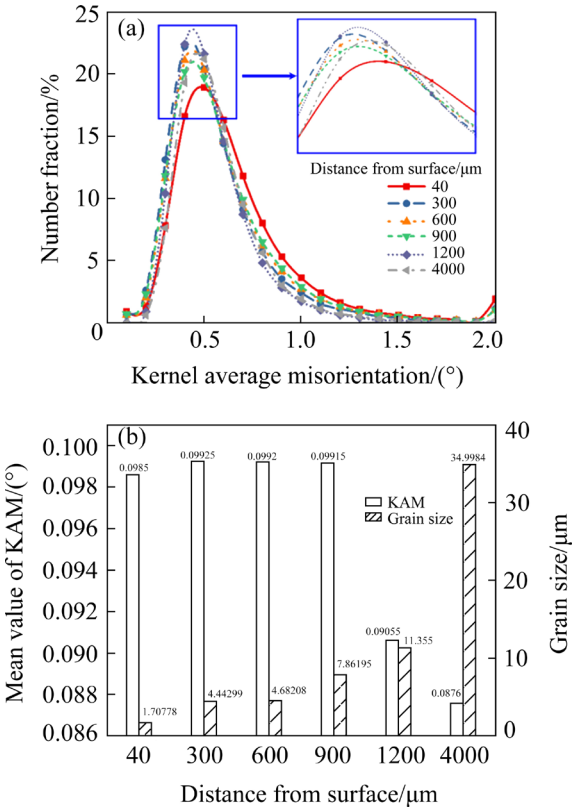

Fig. 15 KAM distribution (a) and mean values of KAM and grain size of regions with different distances from surface (b)

4.3 Interaction of dislocation and precipitates strengthening

Figures 16 and 17 show high- magnification TEM images of the sub-block, where many precipitates are isolated and dispersed in the lath and interface. Dislocations are piled up around the precipitates in Figs. 16(a–c), or cut (Fig. 17(a)) and pass over (Fig. 17(b)), which clearly shows how the precipitates hinder dislocation motion during deformation. When dislocations slide on the slip plane under shear stress, they are pinned at trap points and arch among the dispersed precipitate particles with an arching angle φ. Dislocations can pass over the precipitates when the shear stress exceeds the critical resistance of the obstacle. Dislocations can cut the particle in the case of weak pinning when $\pi/2<\varphi<\pi$. In the case of larger non-deformable precipitates that cannot be cut (strong pinning), dislocations with $\varphi<\pi/2$ can move around the precipitates.

Figure 18 shows a precipitate being cut by a dislocation, where the interfacial area and interfacial energy increase due to the formation of a step dislocation. Assuming that the precipitate is spherical with a radius r and that the dislocations do not cut through the center of the sphere, then the average radius of the cross-section of the precipitate is $\bar{r}=\sqrt{2/3}r$; the average added interfacial area is $\pi\sqrt{(8/3)}rb$, and the energy consumed during cutting is $\pi\sqrt{(8/3)}rb\gamma$. Furthermore, the additional stress ($\Delta\tau$) is given by [39]

$$\Delta\tau=\frac{\pi\sqrt{(8/3)}rb\gamma}{b\bar{l}\bar{r}} \tag{7}$$

Table 4 Parameters used in estimation of strengthening mechanism

Parameter	Value
Hall−Patch constant, k_y/(MPa·μm$^{1/2}$)	400
Elastic modulus, E/GPa	110
Poisson's ratio, V	0.32
Taylor constant, α	0.4
Taylor factor, M_t	3.04651
EBSD constant, u/μm	0.15
Lattice constant, a/nm	0.87

Table 5 Theoretical stress contribution from dislocation and grain boundary strengthening

Distance from surface/μm	σ_{dis}/MPa	σ_{GB}/MPa
40	1020.9	306.16
300	1024	189.77
600	1023	184.9
900	1019.9	176.09

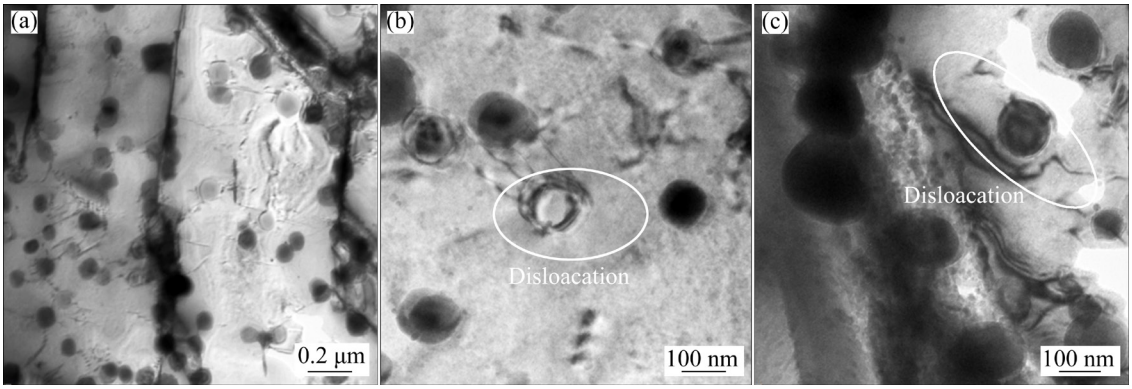

Fig. 16 FTEM micrographs of LNAB specimen: (a) Precipitates distribution within laths; (b, c) Dislocation moving around precipitates

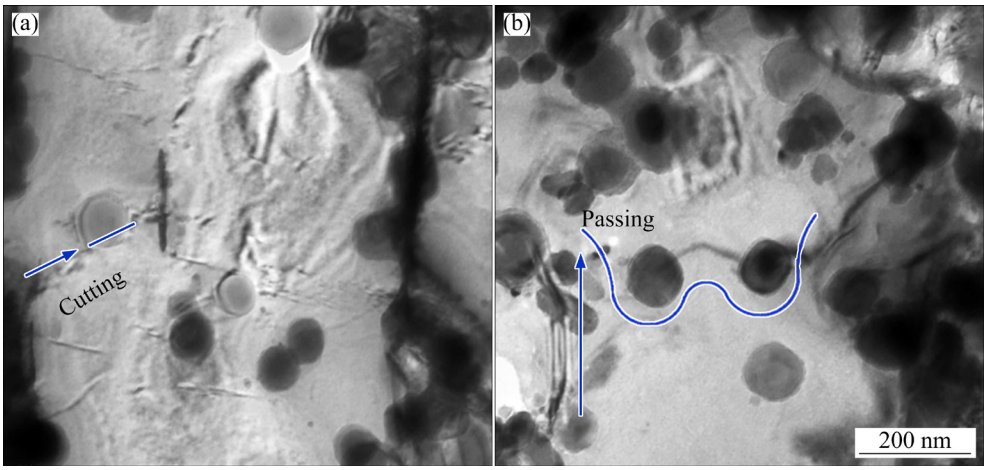

Fig. 17 Dislocations cutting (a) and passing (b) precipitates

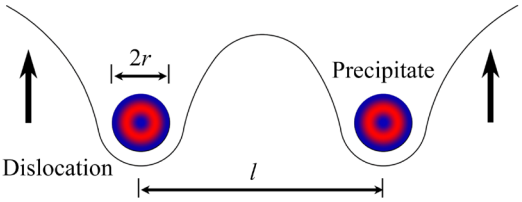

Fig. 18 Schematic diagram of obstruction effect of precipitate on dislocation motion

The average distance between precipitates ($\bar{l}$) is related to the number of precipitates per unit of the slip plane (N_A) as

$$\bar{l} = 1/\sqrt{N_A} \tag{8}$$

In addition, N_A can be expressed as a function of the volume fraction (f):

$$N_A = \frac{f}{\pi \bar{r}^2} = 3f/(2\pi r^2) \tag{9}$$

Therefore, Eq. (7) is simplified by substituting $\bar{l}$ and N_A as

$$\Delta\tau = \frac{2\pi\gamma}{\bar{l}} = \sqrt{\frac{3\pi}{2}}\frac{\gamma f^{1/2}}{r} \tag{10}$$

Then, the precipitate strengthening effect can be predicted during precipitate deformation. Appling Eq. (10) to the data shown in Figs. 16 and 17, the additional stress ($\Delta\tau$) during the cutting can be estimated:

$$\Delta\tau = \sqrt{\frac{3\pi}{2}}\frac{(11.59)^{1/2}\gamma}{40.363} \tag{11}$$

Here, the specific surface energy (γ) is related to the crystal structure at the interface and is estimated from the HRTEM figures considering the thermodynamics and interfacial structure. The lath and precipitate have a coherent interface with the same structure and lattice constant but different chemical compositions. The atoms at the interface are regularly arranged on both sides without lattice

distortion due to the different atomic distances resulting in γ being mainly dependent on changes in the nuclear bond energy, which is generally small (γ=0.01−0.1 J/m^2), and results in $\Delta\tau$ values of 1.8−18 MPa.

While precipitate particles of a specific size cannot be cut, they can be by-passed by the dislocations following Orowan looping mechanism, as shown in Fig. 18. Dislocations passing around a single precipitate require extra energy to overcome the bending tension (τ_p):

$$\tau_p = \alpha \frac{\mu b}{x} \tag{12}$$

where μ is the Lame coefficient, and x is the distance between the precipitate edges, where the precipitate is likely to work as the Frank−Read dislocation source.

When the precipitate density is high, $\bar{l}$ needs to be considered:

$$\Delta\tau = \frac{2\Gamma}{b(\bar{l}-2\bar{r})} = K\frac{\mu_K b}{2\pi(\bar{l}-2\bar{r})}\ln(\frac{\bar{l}-2\bar{r}}{r_0}) \tag{13}$$

where Γ is the line tension of the dislocation, K is a statistical factor related to the dislocation type, μ_K is the average shear modulus related to the contribution from screw and edge dislocations, and r_0 is the dislocation core with r_0=2b. A dislocation loop remains after the dislocation passes over the precipitate, increasing the effective precipitate radius. Therefore, the subsequent dislocation must overcome higher resistance to pass over the precipitate as the passing process strengthens the slip plane.

The $\Delta\tau$ can be calculated by assuming that the difference between the shear modulus and thread tension of edge dislocations and screw dislocations is negligible. Then, b has a direction of 1/2a⟨110⟩, and G is expressed by E/[(2(1+ν)]. In addition, $\bar{l}$ and $\bar{r}$ are related as

$$\bar{l} = 2\bar{r}\left(\sqrt{\frac{\pi}{4f}}-1\right) \tag{14}$$

Then, Eq. (13) can be simplified as

$$\Delta\tau = K\frac{\sqrt{2}E\cdot r_0}{16\pi\bar{r}(1+\nu)(\sqrt{\pi/(4f)}-2)}\cdot \ln\left[\bar{r}\left(\sqrt{\pi/(4f)}-2\right)/r_0\right] \tag{15}$$

By applying Eq. (15) to the data obtained in Figs. 16−18, $\Delta\tau$=419 MPa is obtained. This theoretical value is much greater than that of the cutting mode for the high volume fraction and small grain size of the precipitates, contributing to precipitate strengthening. Therefore, the passing process is much less favorable than the cutting process.

During cavitation, the synergetic effect of dislocation, grain-boundary, and precipitate strengthening mechanisms contributes to delaying cavity crack initiation and extension. At the microscale, dislocation strengthening is the major contributor to strength enhancement besides boundary strengthening. In addition, the particle passing mechanism is less favorable than the cutting mechanism at the nanoscale.

4.4 Enhancing mechanism of LSM on corrosion and cavitation behavior of NAB

The surface morphology and potential surface distribution of NAB and LNAB specimens are obtained by AFM, as shown in Fig. 19. The difference in corrosion sensitivity between NAB and LNAB surface structures is further studied. The difference in surface height of different phases causes the fluctuation of surface morphology. The brighter the surface color is, the larger the height in this area is. The contact potential difference (CPD) and the work functions of the instrument probe and phase surface have the relationship as follows:

$$V_{CPD} = (\Phi_{tip} - \Phi_s)/e \tag{16}$$

where V_{CPD} is the potential difference; Φ_{tip} and Φ_s represent the tip and surface work functions, respectively; e is the unit electron. Then, the surface potential difference of the sample decreases with the increase of work function with constant tip surface work function. Work function refers to the minimum energy required for electrons to escape from the solid surface. The lower the work function is, the higher the surface contact potential difference is, and the closer the color in the figure to red is [40].

The work function is the minimum energy required for the outermost electrons to escape from the surface. The corrosion behavior is related to the work function: the higher the work function is, the higher the minimum energy required for electron detachments is, and the better the corrosion resistance is. The work function of a material is

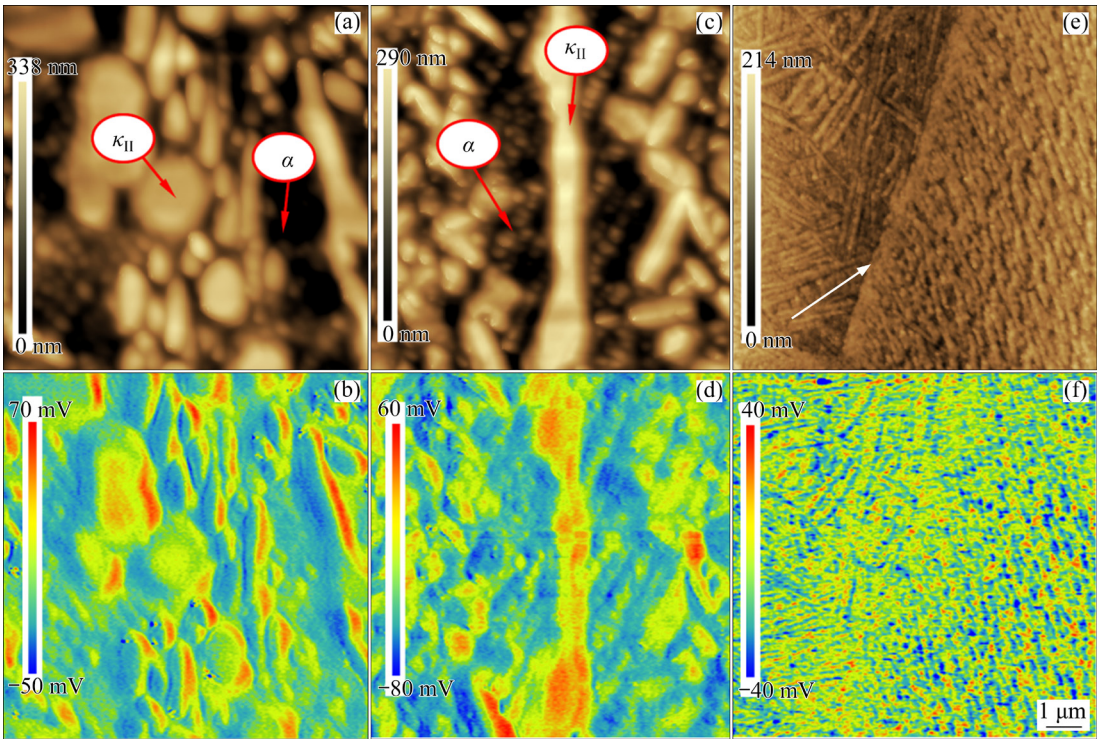

Fig. 19 Potential maps obtained using AFM of NAB (a−d) and LNAB (e, f) specimens: (a, c, e) Surface height difference; (b, d, f) Surface potential difference

closely related to its elemental composition. The following formula is usually used to calculate the theoretical work function (W) of a material:

$$W = \sum_i (W_i \cdot a_i) / (\sum_i a_i) \quad (17)$$

where W_i is the work function of the i element, and the a_i is the content of the i element. The work functions of copper, aluminum, iron, and nickel elements are 4.65, 4.28, 4.5, and 5.15 eV, respectively. Based on the chemical composition of each phase and the work function of the alloy elements in Table 3, the work functions of the κ phases are lower than those of α and β phases as $\kappa_I \approx \kappa_{II} \approx \kappa_{IV} < \kappa_{III} < \alpha \approx \beta$.

As shown in Figs. 19(a, c), the potenial of κ_{II} and κ_{III} phases is higher than that of the α phase. During the grinding and polishing process of sample preparation, the α phase is softer and easier to be removed, while the κ phase is more difficult to polish. As shown in Figs. 19(b, d), the κ_{II} and κ_{III} phases show higher surface contact potentials, and the potential difference is the largest at the boundaries of the α and κ phases. The maximum range can reach 120 and 140 mV, respectively. After LSM treatment, the surface structure transforms into a single martensite structure.

As shown in Figs. 19(e, f), the LNAB surface shows a clear strip martensite phase after electro-polishing and ion etching. The maximum height difference of all surfaces is 219 nm, which is 44% lower than that of NAB surface. The surface contact potential difference exists at the grain boundary; the maximum potential difference range is 80 mV. The homogeneous fine-grained structure of LNAB can further provide reinforcement for the amorphous loops between the dispersed precipitates and laths, which enhances the corrosion resistance, as previously investigated in detail [41,42]. The amorphous loops can reduce the potential difference between the laths and precipitates by providing a transition region in the composite structure, as shown in Fig. 11(d).

The samples, after cavitation, were first inserted in the epoxy resin. After sanding and polishing with the paste, the samples were taken out for electrolytic polishing. Then, the pieces were cleaned with deionized water and dried to observe the cross-section morphology. Figure 20 shows the cross-sectional morphologies of NAB and LNAB specimens after 20 h cavitation. There are a tearing phenomenon on the surface of NAB specimen and holes on the subsurface since the strength difference of the κ and α phase is too large during ultrasonic

impact. In the deformation process, α phase preferential deformation results in gaps forming at the κ phase interface. The continuous ultrasonic shock breaks the κ phase away from the substrate, leaving the holes which can continue to expand along the phase boundaries. The surface roughness of LNAB specimen is smaller than that of NAB specimen, and there are no pores in the subsurface layer, showing mild, uniform cavitation morphology consistent with the surface morphology in Fig. 7.

During cavitation, the bubbles burst on the blades, causing a hammer force and severe damage to the metals. Many studies on cavitation show that metals suffer from mechanical shock and chemical corrosion. The mechanical shock leads to plastic deformation, and the repeated attack eventually produces cavitation pits and material removal. Meanwhile, the corrosive medium makes the metal on the material surface dissolve, making it easier to be tripped. The synergistic effect of the corrosion and mechanical attack dominates the cavitation behavior of the alloys. To investigate the correlation between the cavitation and the corrosion and mechanical behavior, the mass losses resulting from the three mechanism behavior are measured by the cavitation test immersed in 3.5% NaCl solution and deionized water, respectively. The following equation can describe the cavitation mass loss:

$$M_T=M_M+M_C+M_S \tag{18}$$

where M_T is the total mass loss during the cavitation process; M_M is the pure mass loss from the mechanical attack in deionized water; M_C represents the mass loss caused by corrosion dissolution and can be obtained through the polarization curve under static conditions; M_S is the mass loss cased by combined interaction between two processes.

Faraday's law can be used to calculate the value of M_C:

$$M_C=\frac{M_A I}{nF} \tag{19}$$

where M_A is the average molecular mass with a value of 56.34 g/mol, n is the valence electron value with a value of 2, F is the Faraday factor with a value of 96485 C/mol, and I is the corrosion current. Then, the corrosion current of 1 mA causes a mass loss of 1.05 mg/h [43]. The values of the mass losses are given in Table 6, together with the contributions to the mass loss.

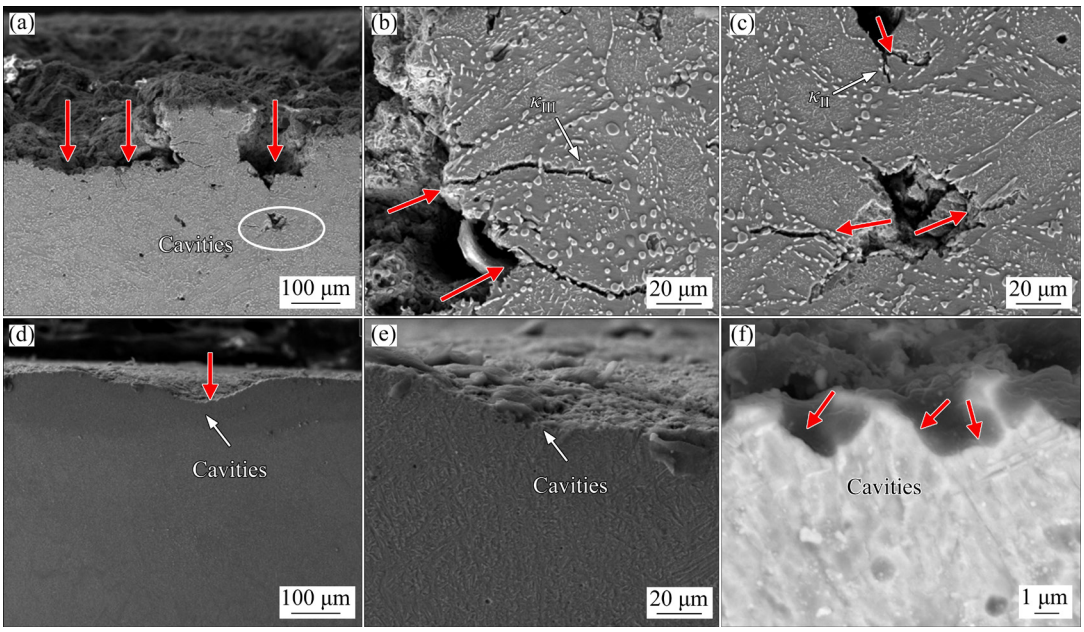

Fig. 20 Cross-sectional morphologies after cavitation for 20 h: (a−c) NAB specimen; (d−f) LNAB specimen

Table 6 Mass losses and contribution for NAB and 3-10 LNAB specimens in 3.5% NaCl solution

Sample	Mass loss/(mg·cm^{-2})				Contribution/%		
	M_T	M_M	M_C	M_S	M_M	M_C	M_S
NAB	16.2	12.9	1.05	2.25	79.62	6.48	13.9
3-10 LNAB	3.27	2.12	0.34	0.81	64.83	10.40	34.77

The mass loss caused by the mechanical attack shows the highest proportion on NAB and LNAB alloys, indicating that the mechanical effect dominates the cavitation damage. The mechanical mass loss of NAB specimen is 6.1 times that of LNAB specimen. This further demonstrates that the enhancement of cavitation resistance of LNAB specimen is due to the improvement of mechanical properties. The higher the strength and hardness are, the more resistant the mechanical impact is. The progress of mechanical properties, such as strength and hardness, is attributed to forming a three-level hierarchy structure: lath, block, and packet. The sub-block consists of laths within diffusely distributed precipitates. During the cavitation process, the synergetic effect of the dislocation, grain boundary, and precipitate strengthening mechanism conduces to postpone the initiation and propagation of cavitation cracks.

Meanwhile, the mass loss of LNAB specimen resulting from corrosion is also lower than that of NAB specimen, indicating that the corrosion resistance is improved. In the cavitation process, the potential difference of each phase in NAB alloy forms galvanic corrosion, and phase-selective corrosion occurs, accelerating the dissolution of metals. When the bubbles impinge on the surface, the phase-selective corrosion areas are peeled off under mechanical attack, forming large cavities. In the meantime, the impact of cavitation brings more oxygen, accelerating the corrosion and dissolution of metals. A single homogeneous martensite structure is formed on the surface of LNAB alloy, which eliminates the galvanic and phase-selective corrosion, reducing the corrosion dissolution rate of metals. Benefiting from the uniform structure, corrosion and cavitation damage synergism is not apparent, exhibiting higher cavitation resistance.

Figure 21 shows the enhancement mechanism of cavitation resistance of NAB alloy by LSM. During cavitation process of NAB alloy, cavities and cracks are preferentially formed on the interfaces of the κ and α phases. The low-strength α phase is preferentially stripped, resulting from selective corrosion and deformation. The small size κ_{II} phase falls from the interfaces to accelerate the expansion of cavities. The deep cavities supply more corrosion area and exposed structure, accelerating the corrosion effect. This accelerated process is consistent with the gradual rise of the slope of the mass loss curve of NAB alloy (Fig. 6(a)), and the cavitation rate is gradually accelerated. During the cavitation process of LNAB alloy, corrosion preferentially occurs at the grain boundary. And the martensite grains are difficult to remove for their high strength, making it challenging to produce large-scale cavities. Therefore, the mass loss occurs by layer-by-layer corrosion and peeling, consistent with the mass loss curve of LNAB alloy (Fig. 7(b)).

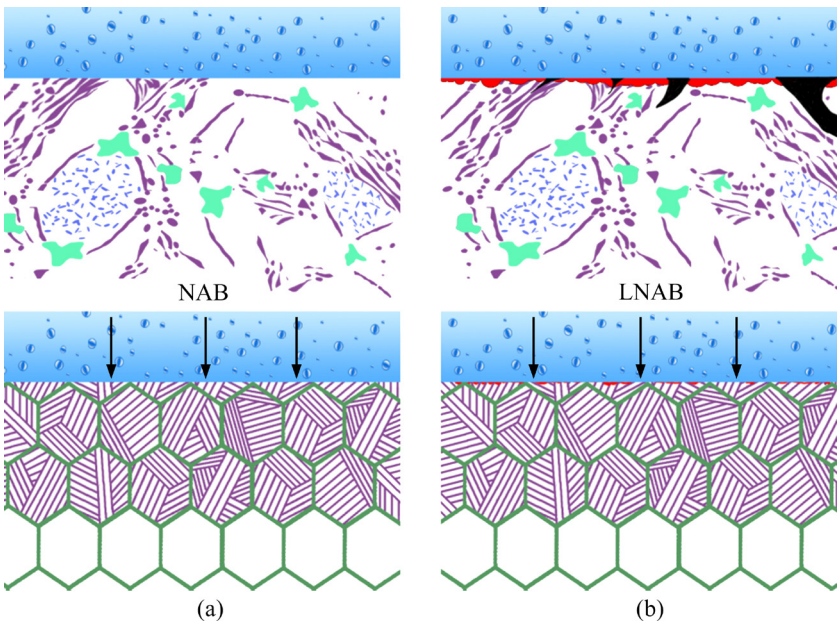

Fig. 21 Strengthening mechanisms of LSM on cavitation behavior: (a) NAB alloy; (b) LNAB alloy

5 Conclusions

(1) LSM induces the refined martensite structure; the average grain size decreases with scanning speed increasing, and laser power decreasing.

(2) After LSM, the specimens show a higher corrosion and cavitation resistance in 3.5% NaCl solution. The optimal parameter of 3 kW and 10 mm/s contributes to the increased corrosion resistance and the reduced mass loss of the NAB specimen.

(3) During the cavitation process, the cavities are more prone to occur in the coarser martensite structure and the heterogeneity phase structure, in which severe cavities expansion appears. In contrast, the cavitation damage is uniform, and the fine martensite structure is prone to be peeled off by layers.

(4) A three-level hierarchical martensite structure of β' is obtained, which comprises packet, block, and lath martensite. Meanwhile, the sub-block consists of laths within sparsely distributed precipitates.

(5) The strength enhancement is attributed to the synergetic strengthening mechanism of high dislocation density, fine-grain reinforcement, and dispersed precipitates. The homogeneous structure reduces the potential difference between the original α and κ phases and eliminates selective corrosion. In addition, the amorphous loops around the nanoscale precipitates contribute to reducing the potential corrosion difference between laths and precipitates to increase the corrosion resistance. The composite mechanism of strength and corrosion resistance enhancement dominates the cavitation process of LNAB.

Acknowledgments

This work was financially supported by the Major State Basic Research Development Program of China (No. 2020YFB2010304) and the National Natural Science Foundation of China (No. 92066202). The authors also acknowledge the technical support from the Analytic Testing Center of Huazhong University of Science and Technology, China.

References

[1] HOWELL P R. Copper brass bronze: On the phases, microconstituents and microstructures in nickel−aluminum bronzes [R]. Hempstead: Copper Development Association, 2013.

[2] MOUSAVI S E, NAGHSHEHJESH N, AMIRNEJAD M, SHAMMAKHI H, SONBOLI A. Corrosion performance and tribological behavior of diamond-like carbon based coating applied on Ni−Al−bronze alloy [J]. Transactions of Nonferrous Metals Society of China, 2021, 31: 499−511.

[3] CARLTON J S. Marine propellers and propulsion [M]. 3rd ed. Oxford: Elsevier, 2012.

[4] KWOK C T, CHENG F T, MAN H C. Synergistic effect of cavitation erosion and corrosion of various engineering alloys in 3.5% NaCl solution [J]. Materials Science and Engineering A, 2000, 290: 145−154.

[5] PREISER H S, TYTELL B H. The electrochemical approach to cavitation damage and its prevention [J]. Corrosion, 1961, 17: 535−549.

[6] AURET J G, DAMM O F, WRIGHT G J, ROBINSON F P A. Influence of cathodic and anodic currents on cavitation erosion [J]. Corrosion Science, 1993, 49: 910−920.

[7] BASUMATARY J, WOOD R J K. Synergistic effects of cavitation erosion and corrosion for nickel aluminum bronze with oxide film in 3.5% NaCl solution [J]. Wear, 2017, 376/377: 1286−1297.

[8] DING Xiang, CHENG Xu-dong, YU Xiang, LI Chao, YUAN Cheng-qing, DING Zhang-xiong, Structure and cavitation erosion behavior of HVOF sprayed multi-dimensional WC−10Co4Cr coating [J]. Transactions of Nonferrous Metals Society of China, 2018, 28: 487−494.

[9] SONG Qi-ning, ZHANG Hui-lin, LI Hao-nan, HONG Hao, XU Nan, ZHANG Gen-yuan, BAO Ye-feng, QIAO Yan-xin. Corrosion and cavitation erosion behaviors of the manganese-aluminum-bronze cladding layer prepared by MIG in 3.5% NaCl solution [J]. Materials Today Communications, 2022, 31: 103566.

[10] LI Yang, LIAN Ying, SUN Yan-jun. Comparison of cavitation erosion behaviors between the as-cast and friction stir processed Ni–Al bronze in distilled water and artificial seawater [J]. Journal of Materials Research and Technology, 2021, 13: 906−918.

[11] LI Yang, LIAN Ying, SUN Yan-jun. Cavitation erosion behavior of friction stir processed nickel aluminum bronze [J]. Journal of Alloys and Compounds, 2019, 795: 233−240.

[12] THAPLIYAL S, DWIVEDI D K. On cavitation erosion behavior of friction stir processed surface of cast nickel aluminum bronze [J]. Wear, 2017, 376/377: 1030−1042.

[13] SUN Yong-an, WANG Hai-bo, LIU Wei, SONG Gup-lin, LI Qiu-lin. Improvement of surface resistance to cavitation corrosion of nickel aluminum bronze by electropulsing-assisted ultrasonic surface rolling process [J]. Surface and Coatings Technology, 2019, 368: 215−223.

[14] COTTAM R, LUZIN V, MOODY H, EDWARDS D, MAJUMDAR A, WONG Y C, WANG J, BRANDT M. The

role of microstructural characteristics in the cavitation erosion behavior of laser melted and laser processed nickel−aluminium bronze [J]. Wear, 2014, 317: 56−63.

[15] HARDES C, PÖHL F, RÖTTGER A, THIELE M, THEISEN W, ESEN C. Cavitation erosion resistance of 316L austenitic steel processed by selective laser melting (SLM) [J]. Additive Manufacturing, 2019, 29: 100786.

[16] ZHANG S, WU C L, ZHANG C H, GUAN M, TAN J Z. Laser surface alloying of FeCoCrAlNi high-entropy alloy on 304 stainless steel to enhance corrosion and cavitation erosion resistance [J]. Optics & Laser Technology, 2016, 84: 23−31.

[17] TANG C H, CHENG F T, MAN H C. Effect of laser surface melting on the corrosion and cavitation erosion behaviors of a manganese–nickel–aluminum bronze [J]. Materials Science and Engineering A, 2004, 373: 195−203.

[18] TANG C H, CHENG F T, MAN H C. Improvement in cavitation erosion resistance of a copper-based propeller alloy by laser surface melting [J]. Surface and Coatings Technology, 2004, 182: 300−307.

[19] MITELEA I, BORDEAŞU I, RIEMSCHNEIDER E, UŢU I D, CRĂCIUNESCU C M. Cavitation erosion improvement following TIG surface-remelting of gray cast iron [J]. Wear, 2022, 496/497: 204282.

[20] KWOK C T, MAN H C, CHENG F T, LO K H. Developments in laser-based surface engineering processes: With particular reference to protection against cavitation erosion [J]. Surface and Coatings Technology, 2016, 291: 189−204.

[21] GB/T 9790—2021. Metallic materials − Vickers and Knoop microhardness tests of metallic and other inorganic coatings [S].

[22] ASTM G5 — 14. Standard test method for making potentiodynamic anodic polarization measurements [S].

[23] ASTM G32—16. Standard test method for cavitation erosion using vibratory apperatus [S].

[24] WILLIAMSON G K, HALL W H. X-ray line broadening from filed aluminum and wolfram [J]. Acta Metallurgica, 1953, 1: 22−31.

[25] LIPSON, H. Elements of X-ray diffraction [J]. Contemporary Physics, 1957, 20: 87−88.

[26] YILBAS B S, TOOR I, MALIK J, PATEL F, KARATAS C. Electrochemical testing of laser treated bronze surface [J]. Journal of Alloys and Compounds, 2013, 563: 180−185.

[27] LV Yu-ting, DING Yan, HAN Yuan-fei, ZHANG Lai-chang, WANG Li-qiang, LU Wei-jie. Strengthening mechanism of friction stir processed and post heat treated NiAl bronze alloy: Effect of rotation rates [J]. Materials Science and Engineering A, 2017, 685: 439−446.

[28] NI D R, XUE P, WANG D, XIAO B L, MA Z Y. Inhomogeneous microstructure and mechanical properties of friction stir processed NiAl bronze [J]. Materials Science and Engineering A, 2009, 524: 119−128.

[29] PIDAPARTI R M, AGHAZADEH B S, WHITFIELD A, RAO A S, MERCIER G P. Classification of corrosion defects in NiAl bronze through image analysis [J]. Corrosion Science, 2010, 52: 3661−3666.

[30] KITAHARA H, UEJI R, TSUJI N, MINAMINO Y. Crystallographic features of lath martensite in low-carbon steel [J]. Acta Materialia, 2006, 54: 1279−1288.

[31] SUIKKANEN P P, CAYRON C, DEARDO A J, KARJALAINEN L P. Crystallographic analysis of martensite in 0.2C−2.0Mn−1.5Si−0.6Cr steel using EBSD [J]. Journal of Materials Science & Technology, 2011, 27: 920−930.

[32] MEYERS M A, CHAWLA K K. Mechanical behaviour of materials [M]. 2nd ed. Cambridgeshire: Cambridge University, 2008.

[33] PANDE C S, COOPER K P. Nanomechanics of Hall−Petch relationship in nanocrystalline materials [J]. Progress in Materials Science, 2009, 54: 689−706.

[34] LIANG Yi-long, LONG Shao-lei, XU Ping-wei, LU Ye-mao, JIANG Yun, LIANG Yu, YANG Ming. The important role of martensite laths to fracture toughness for the ductile fracture controlled by the strain in EA4T axle steel [J]. Materials Science and Engineering A, 2017, 695: 154−164.

[35] IZA-MENDIA A, GUTIÉRREZ I. Generalization of the existing relations between microstructure and yield stress from ferrite–pearlite to high strength steels [J]. Materials Science and Engineering A, 2013, 561: 40−51.

[36] SASTI N, JORGE-BADIOLA D, TAHERI M, URANGA P. Phase transformation study in Nb−Mo microalloyed steels using dilatometry and EBSD quantification [J]. Metallurgical and Materials Transactions A, 2013, 44: 3552−3563.

[37] HE S H, HE B B, ZHU K Y, HUANG M X. On the correlation among dislocation density, lath thickness and yield stress of bainite [J]. Acta Materialia, 2017, 135: 382−389.

[38] UNGÁR T, HARJO S, KAWASAKI T, TOMOTA Y, RIBÁRIK G, SHI Z. Composite behavior of lath martensite steels induced by plastic strain, a new paradigm for the elastic-plastic response of martensitic steels [J]. Metallurgical and Materials Transactions A, 2016, 48: 159−167.

[39] ARGON A S. Strengthening mechanisms in crystal plasticity [M]. 1st ed. Massachusetts: Oxford University Press, 2008.

[40] SONG Q N, ZHENG Y G, NI D R, MA Z Y. Studies of the nobility of phases using scanning Kelvin probe microscopy and its relationship to corrosion behavior of Ni−Al bronze in chloride media [J]. Corrosion Science, 2015, 92: 95−103.

[41] ZHANG B, CHEN Y G, GUO H B. Effects of annealing on structures and properties of Cu−Hf−Al amorphous thin films [J]. Journal of Alloys and Compounds, 2014, 582: 496−499.

[42] SURIANI A B, ALFARISA S, MOHAMED A, KAMARI A, HASHIM N, ISA I M, MAMAT M H, MALEK M F, AHMAD M K. Amorphous Al−Cu alloy nanowires decorated with carbon spheres synthesized from waste engine oil [J]. Journal of Alloys and Compounds, 2015, 642: 111−116.

[43] HONG Yu, ZHENG Yu-gui, YAO Zhi-ming. Cavitation erosion corrosion behaviour of manganese-nickel-aluminum bronze in comparison with manganese-brass [J]. Journal of Materials Science and Technology, 2009, 6: 758−766.

激光表面熔凝对镍铝青铜组织演变和空蚀行为的影响

曾思琪，田静静，胡树兵，肖 明，彭 博

华中科技大学 材料科学与工程学院 材料成形与模具技术国家重点实验室，武汉 430074

摘 要：采用激光表面熔凝对镍铝青铜进行表面强化以提高其抗空蚀性能。通过 XRD、SEM 和 TEM 等手段对微观结构进行表征，并在超声空泡试验机上进行空泡测试。结果表明：采用功率为 3 kW 和扫描速度为 10 mm/s 的激光参数时，耐蚀性和抗空蚀性能较铸态合金得到提高。熔凝处理过程中晶粒细化强化、位错强化和析出相强化的协同强化机制以及均匀组织消除选相腐蚀主导了熔凝后镍铝青铜的抗空蚀性能。

关键词：镍铝青铜；激光表面熔凝；析出相；位错

(Edited by Bing YANG)